JGR Solid Earth

RESEARCH ARTICLE

Key Points:

- In the upper mantle iron oxidation in olivine is a nonmonotonic function of depth and water with maximum oxidation at ~100 km depth
- Iron oxidation is small but can control the concentration of Mg and Si vacancies and thus properties dependent upon these concentrations
- These vacancies are thus predicted to vary nonmonotonically and by several orders of magnitude across the depth range of the upper mantle

Correspondence to:

J. M. R. Muir and F. Zhang,
j.m.r.muir@mail.gyig.ac.cn;
zhangfeiwu@mail.gyig.ac.cn

Author Contributions:

Conceptualization: Joshua M. R. Muir, Michael Jollands
Formal analysis: Joshua M. R. Muir, Michael Jollands
Funding acquisition: Joshua M. R. Muir, Feiwu Zhang
Investigation: Joshua M. R. Muir
Methodology: Joshua M. R. Muir
Project Administration: Feiwu Zhang
Software: Joshua M. R. Muir
Supervision: Feiwu Zhang
Validation: Joshua M. R. Muir
Writing – original draft: Joshua M. R. Muir
Writing – review & editing: Michael Jollands

The Oxidation States of Iron in Dry and Wet Olivine: A Thermodynamic Model

Joshua M. R. Muir[1] , **Michael Jollands[2]** , **and Feiwu Zhang[1]**

[1]State Key Laboratory of Ore Deposit Geochemistry, Institute of Geochemistry, Chinese Academy of Sciences, Guiyang, China, [2]Gemological Institute of America, New York, NY, USA

Abstract The oxidation state of iron in olivine is an important control on many of its properties but is poorly constrained in mantle conditions. In this work Density Functional Theory is used to build a thermodynamic model of Fe oxidation states and incorporation mechanisms as a function of silica activity (αSiO_2), pressure (P), temperature (T), oxygen fugacity (fO_2), and the concentrations of Fe, H_2O, Ti, and Al. Total $Fe^{3+}/\sum Fe$, Fe oxidation pathways and by-products of Fe oxidation (such as Mg and Si vacancies) have a complex dependence upon αSiO_2, P, T, and fO_2, which are difficult to capture using simple Arrhenius relations and experiments over limited ranges. Our model predicts that in the conditions of the upper mantle, depth is the strongest control on $Fe^{3+}/\sum Fe$ and that this relationship is strongly nonmonotonic and varies over several orders of magnitude. $Fe^{3+}/\sum Fe$ is predicted to always be low reaching a maximum of 0.003 at around 100 km depth under normal mantle conditions though the presence of large amounts of water could increase this value further (0.03 with 500 ppmw water). While the Ferric iron concentration is predicted to be low, the concentration of Mg and Si vacancies—and thus vacancy dependent properties such as diffusion and likely strength—are predicted to be primarily a function of iron oxidation. These properties are predicted to vary by multiple orders of magnitude across the depth range of the upper mantle and thus olivine is predicted to have highly dynamic rather than static properties.
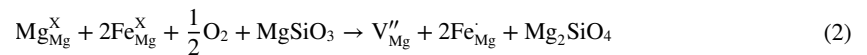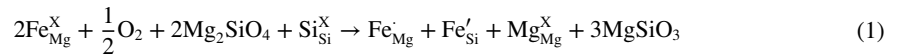
Plain Language Summary Olivine is one of the most important minerals in Earth's mantle and contains significant amounts of iron but we do not accurately know the oxidation state of this iron or how it varies as conditions in the Earth vary. This is important because this oxidation state can control the properties of olivine and thus of the Earth. In this work we use first principles calculations to determine the conditions under which oxidized iron in the 3+ state (ferric iron) is favored. We find that this is complicated with pressure, temperature and the amount of oxygen, silica, alumina and water present having nonmonotonic effects on the ferric iron concentration and that ferric iron concentration can vary by multiple orders of magnitude across the Earth's depth. In the conditions of the Earth's mantle we predict that ferric iron concentration peaks at about 100 km depth and will always be a low percentage of total iron (<0.3% in normal olivine, <3% in wet olivine). The production of ferric iron also produces large amounts of Mg and Si vacancies, however, which will affect certain properties such as diffusion, conductivity and strength in olivine and these are predicted to vary greatly with depth.

1. Introduction

We predict that iron oxidation in mantle olivine is highly variable and nonmonotonic. Its primary controls are predicted to be depth and water concentration and it is predicted to behave extremely differently at high pressures than it does at low pressures. This means that extrapolations of olivine behaviors from low pressure measurements are likely to be unreliable. While iron oxidation is small it impacts heavily upon the vacancy concentration of olivine and thus upon any olivine properties that depend upon these vacancy concentrations. These properties could see significant multi-order of magnitude variation across mantle depths based purely upon iron oxidation and any interaction it has with water. The oxidation state of iron in olivine is an important control on many properties such as conductivity (Dai & Karato, 2020), melting (Blundy et al., 2020; Davis & Cottrell, 2021), water content (Babushkina et al., 2009), magnetization (Knafelc et al., 2019), elasticity (Cline et al., 2018), deformation (Mackwell, 2008) and the formation of other phases such as hematite. Thus determining this oxidation state in upper mantle conditions and how it varies as these conditions (such as pressure, temperature and oxygen fugacity) vary is important for understanding the properties of the upper mantle. The ratio of Ferric iron to total iron (Fe^{3+}/Fe^{tot}) has been measured in numerous xenoliths and found to be near or

below the detectability of Mössbauer spectroscopy ($\sim$0.00–0.06) (Banfield et al., 1990; Canil et al., 1994; Ejima et al., 2012, 2013, 2018; McGuire et al., 1991). This makes it difficult to reliably constrain Ferric iron in olivine with such measurements.

Both of these problems can be avoided with a thermodynamic model of the oxidation process of iron in olivine. This would allow precise estimations of Fe^{3+}/Fe^{tot} and how it varies across possible mantle conditions. To determine the thermodynamics of oxidation the mechanism of oxidation needs to be known. This has been previously speculated (Dohmen and Chakraborty, 2007) to occur through two reactions:

$$2Fe_{Mg}^X + \frac{1}{2}O_2 + 2Mg_2SiO_4 + Si_{Si}^X \rightarrow Fe_{Mg}^{\cdot} + Fe_{Si}' + Mg_{Mg}^X + 3MgSiO_3 \tag{1}$$

$$Mg_{Mg}^X + 2Fe_{Mg}^X + \frac{1}{2}O_2 + MgSiO_3 \rightarrow V_{Mg}'' + 2Fe_{Mg}^{\cdot} + Mg_2SiO_4 \tag{2}$$

These and all such reactions in our paper will be presented in Kroger-Vink notation (Kroger & Vink, 1956). In short the large text represents an atom or a vacancy (V), the subscript represents the site in the crystal where it is found (with i for an interstitial site) and the superscript represent the formal charge with $\prime$ for a negative charge, $\bullet$ for a positive charge and X for a neutral charge. Both of these reactions require the interaction of the olivine crystal with some external reactant. Equivalent forms could be written with SiO_2 or MgO through using the equivalence of SiO_2 plus MgO to $MgSiO_3$. These reactions can only occur in a thermodynamically open system and at a shrinking (Equation 1)/growing (Equation 2) crystal interface and will be rate limited by Mg and Si diffusion (Equation 1) or solely by Mg diffusion (Equation 2). A thermodynamically partially closed reaction which does not require external products/reactants can be considered by combining these two reactions:

$$8Fe_{Mg}^X + 2O_2 + Si_{Si}^X + 2Mg_{Mg}^X \rightarrow 3V_{Mg}'' + 7Fe_{Mg}^{\cdot} + Fe_{Si}' + Mg_2SiO_4 \tag{3}$$

This reaction still requires a source of oxygen and expands the crystal 1 Mg_2SiO_4 unit and thus it is not strictly closed. These three mechanisms produce Ferric iron located on different sites and produce different amounts of Mg vacancies and so—assuming no other oxidation mechanisms are present- can be quantified against each other. Thermogravimetric measurements were performed by Nakamura and Schmalzried (1983) and Tsai and Dieckmann (2002) to determine defect concentrations and these were then converted into a thermodynamic model of oxidation in Dohmen and Chakraborty (2007). This model predicts that across an fO_2 olivine stability range $[Fe_{Mg}^{\cdot}]$, $[Fe_{Si}']$ and $\left[V_{Mg}''\right]$ are around 0.1 ppm to 1 parts per thousand with slightly more $Fe_{Mg}^{\cdot}$ produced than Fe_{Si}'. There are limitations with this approach however. The concentration of Ferric iron and Mg vacancies in olivine is very small requiring extreme precision in measurements and this is demonstrated in Dohmen and Chakraborty (2007) where the two different experimental data sets lead to different predictions of activation energies, in some cases with opposite signs. The exact activity of αSiO_2 in the experiments is unclear and this will clearly be important when considering the form of typical oxidation reactions such as Equations 1 and 2. The model of Dohmen and Chakraborty (2007) was done based on measurements at atmospheric pressure and over a limited temperature range (1273–1553 K) and a wider range of pressure and temperature needs to be considered. Finally fitting reaction parameters to a set of modeled masses is problematic and requires a large set of assumptions. This is most prominently seen in the model of Dohmen and Chakraborty (2007) where all reactions are modeled with fixed K (equilibrium constant) values. This is an approximation that must break down at some point, particularly when the concentration of defects decreases and configurational entropy effects become more important. Fixed ideal K values based on fitting to some measured values also make extrapolation of results across different conditions (such as P, T, fO_2, Fe#, and αSiO_2) difficult as the fitting of K and the assumptions behind that fitting increasingly break down as the conditions move away from those where the measurements were taken.

In this study, a similar model was built, but from first principles. Density functional theory (DFT) was used to calculate the energy of Equations 1–3 as well as other relevant defect reactions and then these reactions were solved for thermodynamic equilibrium. This was done over a wide range of Fe#, P, T, fO_2, and αSiO_2 conditions, as well as in the presence of H_2O, Ti, and Al.

2. Method

2.1. Units and Definitions

All temperatures (T) are in K, all pressures (P) in GPa, corrected with a linear correction to experimental volumes with the method given in Muir et al. (2021). Total Fe is presented as Fe# ([Fe]/[Fe]+[Mg]). All water concentrations are given as $[H_2O]_{bulk}$ in ppmw. Oxygen fugacity fO_2 is presented in log bar units. We present our results at oxygen fugacity values relative to a FMQ buffer which requires us to know this value at arbitrary T and P. FMQ values at arbitrary P and T were taken from O'Neill (1987) and adjusted for pressure using the molar volumes of Holland and Powell (2011). It is important to consider what values fO_2 takes in the Earth. fO_2 values gradually decrease with depth and can go from ~FMQ+2 to ~FMQ-6 with considerable lateral heterogeneity also possible (Frost & McCammon, 2008). For Figures 4–6 our model uses a relationship of FMQ versus depth that was adapted from Frost and McCammon (2008) (Figure S1 and Table S1 in Supporting Information S1).

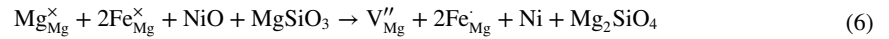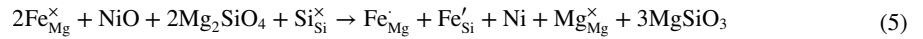### 2.2. Thermodynamic Model

A thermodynamic model of defects in olivine was previously built for Fe-free, H-bearing forsterite in Muir, Jollands, et al. (2022), and here is extended using the same methods but with additional terms to cover Fe. A full explanation of the method is given in Muir, Jollands, et al. (2022) but we shall discuss the basic logic here with more details in the supplementary information. Similarly, the most important chemical equations shall be discussed here but a full list of equations used is given in the supplementary information.

In short, the method uses free energy minimization to find the equilibrium concentration of defects. In each case we use DFT to calculate the energy of adding a defect to a forsterite supercell with 112 atoms- a much larger concentration than occurs in real systems. We then assume ideal mixing (the non-configurational entropy is a linear function of the concentration) and calculate the configurational entropy via analytical methods and incorporate enthalpy penalties for defect mixing on unfavored sites and with unfavored geometries. This then allows us to calculate the free energy of any defect as a function of concentration. In Muir, Jollands, et al. (2022) the defects V''_{Mg}, $Mg^{\cdot\cdot}_i$, V''''_{Si}, $Al^{\cdot}_{Mg}$, Al''_{Si}, $\{Al^{\cdot}_{Mg}Al'_{Si}\}^{\times}$, $\{Al^{\cdot}_{Mg}Al^{\cdot}_{Mg}V''_{Mg}\}^{\times}$ and $Ti^{\times}_{Si}$ were examined, alongside some H-bearing defects $(2H)^{\times}_{Mg}$, $(4H)^{\times}_{Si}$, $\{Ti^{\cdot\cdot}_{Mg}(2H)''_{Si}\}^{\times}$, H'_{Mg}, $H^{\cdot}_i$ and $(3H)'_{Si}$. In this work we shall add in the defects Fe^{X}_{Mg}, $Fe^{\cdot}_{Mg}$, Fe'_{Si}, $\{Fe^{\cdot}_{Mg}Fe'_{Si}\}$, $Fe^{\cdot}_I$, $Fe^{\cdot\cdot}_I$ and $\{Fe^{\cdot}_{Mg}Fe^{\cdot}_{Mg}V''_{Mg}\}^{\times}$ representing Fe^{2+} on a M site, Fe^{3+} on Mg and Si sites but not associated with their charge pair, a pair of associated Fe^{3+} on M and Si sites, Ferrous and Ferric interstitials and a complex of $2Fe^{3+}$ and a M vacancy. The {} braces represent associated defects where each species is on a nearest or next-nearest neighbor to another species of the defect. The H bearing defects $\{Fe^{\cdot}_{Mg}H'_{Mg}\}^{\times}$, $\{Fe^{\cdot}_{Mg}(3H)'_{Si}\}$ and $\{Fe'_{Si}H^{\cdot}_i\}$ defects were also considered. All three of these defects were produced to some degree in our modeling but $\{Fe^{\cdot}_{Mg}H'_{Mg}\}^{\times}$ was always the most favored defect due to its much lower energies of formation. These defects can exist on multiple sites (Mg defects on M1 and M2 sites, Fe interstitials on M1, M2, I1, and I2 sites while Si defects only have a single possible site). The enthalpies of each defect on each possible site as a function of pressure were calculated, these are listed in Table S2 in Supporting Information S1. For $\{Fe^{\cdot}_{Mg}Fe'_{Si}\}$ and $\{Fe^{\cdot}_{Mg}H'_{Mg}\}^{\times}$ all possible arrangements with the defect atoms on nearest neighbor sites and with the hydrogen bound to every possible oxygen in the defect were calculated (Tables S3 and S4 in Supporting Information S1). The concentration of $\{Fe^{\cdot}_{Mg}Fe^{\cdot}_{Mg}V''_{Mg}\}^{\times}$ was always predicted to be small (it never exceeded 2×10^{-12} defects/f. u. in the conditions of Figures 4–6) and so for this species only the lowest enthalpy arrangement was used. This arrangement has $Fe^{\cdot}_{Mg}$ then V''_{Mg} then $Fe^{\cdot}_{Mg}$ in a straight line along [001] on an M1 chain. The lowest enthalpy arrangement for each defect was taken at each pressure and its high temperature energy was then calculated using a Quasi-Harmonic Approximation (QHA) method as outlined in Muir, Jollands, et al. (2022) and the supplementary methods.

To calculate the energy of Equations 1–3 requires calculating the energy of an O_2 gas. This value is difficult to obtain accurately in DFT and so instead our model combines Equations 1 and 2 with a NiO/Ni buffering reaction:

$$NiO \rightarrow Ni + \frac{1}{2}O_2 \qquad (4)$$

This rewrites our oxidation reactions with Ni and NiO solids which can be calculated reliably in DFT:

$$2Fe^{\times}_{Mg} + NiO + 2Mg_2SiO_4 + Si^{\times}_{Si} \rightarrow Fe^{\cdot}_{Mg} + Fe'_{Si} + Ni + Mg^{\times}_{Mg} + 3MgSiO_3 \tag{5}$$

$$Mg^{\times}_{Mg} + 2Fe^{\times}_{Mg} + NiO + MgSiO_3 \rightarrow V''_{Mg} + 2Fe^{\cdot}_{Mg} + Ni + Mg_2SiO_4 \tag{6}$$

The energies of Ni and NiO were calculated with DFT + U ($U_{eff} = 5.7$ determined using a linear response formalism). To confirm the reliability of this system we calculated the energy of the following reaction:

$$NiO + Mg \rightarrow Ni + MgO \tag{7}$$

At 0 GPa and static conditions we calculated the reaction enthalpy to be -3.71 which to two decimal places is the same value (-3.71 eV) that is obtained when Equation 7 is calculated from standard enthalpies of formation (NiO:244.3, MgO -601.60 kJ/mol) (Lide, 2010).

The energies of Equations 5 and 6 are thus relative to an NNO buffer. To obtain the energy at an arbitrary fO$_2$ value our model uses Equation 8:
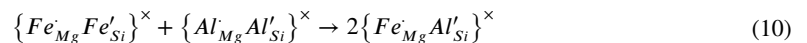
$$dG = d\mu = k_b T d \ln fO_2 \tag{8}$$

where G is the free energy, μ is the chemical potential, k_b is the Boltzmann constant, T is the temperature and fO$_2$ is the oxygen fugacity with d being the variation in that fugacity from the value of the NNO buffer. The fugacity of the NNO buffer at the relevant pressure and temperature was defined by the fitting of Campbell et al. (2009) and then dG was determined between this fugacity and the desired fugacity using Equation 1 and the result added to the energies of Equations 5 and 6.

Once Ferric iron is created it can react to form other species, unlike Equations 5 and 6 these reactions can occur inside the crystal and will not be as limited by diffusion.

$$Fe^{\cdot}_{Mg} + Fe'_{Si} \rightarrow \left\{ Fe^{\cdot}_{Mg} Fe'_{Si} \right\}^{\times} \tag{9}$$

This reaction determines the binding energy of Ferric iron pairs which is the amount of energy they gain from being placed on adjacent crystallographic sites rather than being spread randomly through the crystal. For reactions 9, 13, 17, and 19 below we have defined this associative reaction through two points- one with the atoms in the arrangement with the lowest enthalpy/highest binding energy and one with the atoms infinitively separated (calculated in separate unit cells). We assume these are the two thermodynamic endpoints with an array of intermediate energies in-between the fully associated and fully dissociated states. These intermediate points will be important in the kinetics of Equation 9 and similar reactions and may have non-negligible populations in real samples. Therefore they need to be considered if the average $Fe^{\cdot}_{Mg} - Fe'_{Si}$ distance or the kinetics are to be calculated but in this study we only consider the thermodynamics and thus approximate these middle populations through the equilibrium distribution of the two end points.

The presence of trivalent Al, present as Al(III) pairs on an Mg and an Si site, allows the creation of Fe(III)Al(III) pairs:

$$\left\{ Fe^{\cdot}_{Mg} Fe'_{Si} \right\}^{\times} + \left\{ Al^{\cdot}_{Mg} Al'_{Si} \right\}^{\times} \rightarrow 2 \left\{ Fe^{\cdot}_{Mg} Al'_{Si} \right\}^{\times} \tag{10}$$

It is possible to place Al on the Mg site and Fe on the Si site but this was found to be enthalpically less favorable (+0.6 eV at 0 GPa for reaction 10) and so was ignored.

$$Fe^{\times}_{Mg} \rightarrow V''_{Mg} + Fe^{\cdot\cdot}_I \tag{11}$$

$$Fe^{\cdot}_{Mg} \rightarrow V''_{Mg} + Fe^{\cdot\cdot\cdot}_I \tag{12}$$

These two reactions control the creation of Ferrous and Ferric interstitials.

$$2Fe^{\cdot}_{Mg} + V''_{Mg} \rightarrow \left\{ Fe^{\cdot}_{Mg} Fe^{\cdot}_{Mg} V''_{Mg} \right\}^{\times} \tag{13}$$
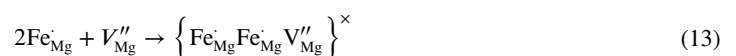
This reaction controls the formation of an iron-vacancy-iron complex. A potential partial binding system with a single Ferric iron and a Mg vacancy is possible but has not been examined in this work.

Non-iron intrinsic defects are included in the model and their formation reactions and energies are all listed in Muir, Jollands, et al. (2022). While all of the listed reactions in that work are included in the model only two of these reactions will prove to be important in this study (producing significant quantities of defects), the Mg Frenkel defect reaction:
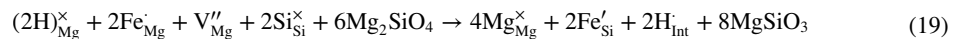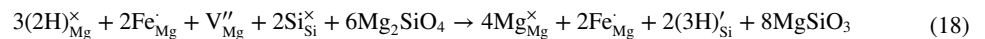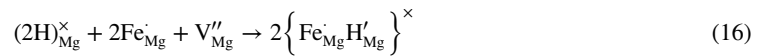
$$\mathrm{Mg_{Mg}^{\times} \rightarrow V_{Mg}'' + Mg_I^{\cdot\cdot}} \tag{14}$$

and a reaction that converts Mg vacancies into Si vacancies:

$$\mathrm{2V_{Mg}'' + Si_{Si}^{\times} + 3Mg_2SiO_4 \rightarrow V_{Si}'''' + 2Mg_{Mg}^{\times} + 4MgSiO_3} \tag{15}$$
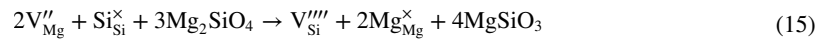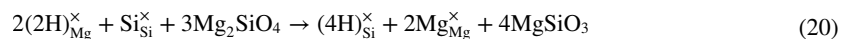
This reaction again requires a crystal surface and so it could be kinetically limited by diffusion but this is not considered in our model.

We also consider the effect of hydrogen. This is done through adding in the following iron hydrogen reactions:

$$\mathrm{(2H)_{Mg}^{\times} + 2Fe_{Mg}^{\cdot} + V_{Mg}'' \rightarrow 2\left\{Fe_{Mg}^{\cdot}H_{Mg}'\right\}^{\times}} \tag{16}$$

$$\mathrm{\left\{Fe_{Mg}^{\cdot}H_{Mg}'\right\}^{\times} \rightarrow Fe_{Mg}^{\cdot} + H_{Mg}'} \tag{17}$$

$$\mathrm{3(2H)_{Mg}^{\times} + 2Fe_{Mg}^{\cdot} + V_{Mg}'' + 2Si_{Si}^{\times} + 6Mg_2SiO_4 \rightarrow 4Mg_{Mg}^{\times} + 2Fe_{Mg}^{\cdot} + 2(3H)_{Si}' + 8MgSiO_3} \tag{18}$$

$$\mathrm{(2H)_{Mg}^{\times} + 2Fe_{Mg}^{\cdot} + V_{Mg}'' + 2Si_{Si}^{\times} + 6Mg_2SiO_4 \rightarrow 4Mg_{Mg}^{\times} + 2Fe_{Si}' + 2H_{Int}^{\cdot} + 8MgSiO_3} \tag{19}$$

All of these have been constructed with Ferric iron on the Mg site charge balanced by a vacancy. Equivalent forms with Ferric iron beginning as a Mg-Si pair $\left\{Fe_{Mg}^{\cdot}Fe_{Si}'\right\}^{\times}$ can be constructed through applying Equations 5 and 6 to these reactions as they are state functions and the path taken to the final product is irrelevant thermodynamically. This is in fact how our model works as it searches for endpoints by applying all reactions both forwards and backwards. Reaction 16 creates $\left\{Fe_{Mg}^{\cdot}H_{Mg}'\right\}^{\times}$ which is the species predicted by Berry et al. (2007) based on FTIR spectra and (Equation 17) is its dissociation reaction. Reaction 18 produces $\left\{Fe_{Mg}^{\cdot}(3H)_{Si}'\right\}^{\times}$ and Equation 19 is its dissociation reaction while Equation 20 produces a Ferric iron on a silicon site with a hydrogen interstitial. Attempting to place the Ferric iron and the hydrogen on the same Si site in the manner of boron (Muir, Chen, et al., 2022) produced a very unstable structure due to the size of the iron atom. Generally our model predicts $\left\{Fe_{Mg}^{\cdot}H_{Mg}'\right\}^{\times}$ to be the most favorable species but the other iron hydrogen species can be produced in non-negligible quantities particularly as the pressure increases.

We also add in all more H based reactions from Muir, Jollands, et al. (2022) the most important of which are:

$$\mathrm{2(2H)_{Mg}^{\times} + Si_{Si}^{\times} + 3Mg_2SiO_4 \rightarrow (4H)_{Si}^{\times} + 2Mg_{Mg}^{\times} + 4MgSiO_3} \tag{20}$$

$$\mathrm{(2H)_{Mg}^{\times} + Ti_{Si}^{\times} \rightarrow \left\{Ti_{Mg}^{\cdot\cdot}(2H)_{Si}''\right\}^{\times}} \tag{21}$$

which control the distribution of the primary non-Fe Hydrogen defects $(2H)_{Mg}^{\times}$, $(4H)_{Si}^{\times}$ and $\left\{Ti_{Mg}^{\cdot\cdot}(2H)_{Si}''\right\}^{\times}$.

Our finding is that oxidation in olivine is a thermodynamically open process- it is controlled by reactions with an external buffer. In our model the control exerted on olivine is dependent upon the αSiO_2 of the buffer. All systems above are presented with an enstatite formalism which represents an αSiO_2 equivalent to the forsterite/enstatite buffer. This buffering is directly relevant for the energies of the reactions above that produce/consume enstatite but as all defect concentrations in a real crystal are interlinked through configurational entropy the identity of any buffer can affect the concentration of all defects even those that do not interact directly with them. It is possible for other SiO_2 activities to occur in the earth and particularly in lab conditions where MgO is a common buffer. This is simulated in our model by applying the following reaction:

$$\mathrm{Mg_2SiO_4 \rightarrow MgO + MgSiO_3} \tag{22}$$

Table 1
Energies (in eV/fu) of the Different Reactions at Different Pressures and Temperatures

	0 GPa			5 GPa			10 GPa		
	1000 K	1500 K	2000 K	1000 K	1500 K	2000 K	1000 K	1500 K	2000 K
(5)	2.579	2.443	2.452	3.210	2.856	2.692	4.832	4.247	4.007
(6)	3.938	3.878	3.808	4.598	4.734	4.758	5.914	5.541	6.417
(8)	−1.394	−1.654	−1.906	−1.717	−2.089	−2.406	−2.117	−2.648	−3.084
(9)	−2.372	−3.190	−3.781	−2.670	−3.547	−4.325	−3.072	−3.876	−4.730
(10)	5.605	5.517	5.511	5.288	5.025	4.903	4.867	4.365	4.050
(11)	6.489	6.064	5.779	6.680	6.118	5.562	7.099	6.538	5.870
(12)	−1.316	−0.832	−0.375	−2.142	−1.740	−1.248	−3.102	−2.905	−2.518
(13)	5.960	5.661	5.368	6.375	6.180	5.939	6.918	6.877	6.747
(14)	5.622	5.335	5.161	5.226	4.742	4.354	4.855	4.202	3.625
(15)	−3.986	−4.008	−3.959	−4.117	−4.504	−4.489	−4.593	−4.8967	−5.784
(16)	5.374	5.609	5.724	5.220	5.521	5.765	5.185	5.481	5.774
(17)	0.571	0.025	−0.559	0.813	0.371	−0.221	1.142	0.901	0.374
(18)	6.917	7.063	6.818	7.508	7.982	7.846	7.946	8.962	9.109
(19)	−1.337	−2.139	−3.376	−1.336	−2.119	−3.672	−1.337	−1.794	−3.413
(20)	−1.031	−1.169	−1.281	−1.045	−1.183	−1.296	−1.006	−1.150	−1.272
(21)	0.270	0.282	0.298	0.239	0.254	0.269	0.231	0.258	0.278

in appropriate amounts. Arbitrary αSiO_2 activity can be obtained through appropriate amounts of Equation 22 but in this work we shall only consider the MgO and $MgSiO_3$ end member cases to show the control of αSiO_2 on this system. In real mantle systems the other minerals can interact with olivine in more ways than are represented here. It is unclear, however, of any reaction that they could induce which would control olivine oxidation outside of αSiO_2 reactions, which are included here, and the partitioning of Fe and H. Fe and H partitioning to other minerals is not included in our model but the effect of such a mechanism would be simply to change the concentration of Fe and H in the olivine itself.

The energy of each defect was determined at the appropriate temperature and pressure using CASTEP (Clark et al., 2005) and a QHA method outlined in the supplementary materials. The energy of each reaction above was then calculated (Table 1). Each reaction was then assigned a variable from 0 to 1 with 0 representing no reaction and 1 representing a reaction going completely to the right. Each combination of variables thus produces a set of concentrations for each defect. The free energy (G) of that concentration of defects was then calculated by the following reaction:

$$\Delta G = \sum_{i=1}^{n} \Delta E_i x_i - TS_{conf} \tag{23}$$

The first term is the energy (E_i) of each of the reactions (i) multiplied by its variable (x_i) (this assumes each reaction has ideal mixing). The second term is a configurational entropy term (S_{conf}) that considers the configurational entropy of all defects simultaneously. The logic and equations behind this are presented in Muir, Jollands, et al. (2022), this work simply adds in additional terms for the different iron containing defects. Each defect has different arrangements of its component atoms and our model uses the enthalpies calculated in Tables S2–S4 in Supporting Information S1 to apply enthalpy penalties to each arrangement. These enthalpy penalties are then used in a Gibbs entropy calculation to determine S_{conf}. The x_i values were then modified, in order to search for the lowest possible energy of Equation 23. Modifying the variables modifies the concentration of defects that are produced from the crystal but the concentration of trace elements (Fe, Ti, Al, or H) was always fixed. As in Muir, Jollands, et al. (2022) a brute force approach was used, wherein each of the variables was varied in order of their favourability and this was continued until the energy of the system remained within 1 peV/unit cell. This method could become trapped in local minima but due to the wide energy differences

between different reactions this is not expected to be a problem except for minor defects with concentrations that are much smaller than those of the major defects. The concentration of these minor defects is not well constrained either in our model or in reality. Small changes to the concentrations of the major defects can have very large effects on the concentrations of the minor defects and thus they are extremely sensitive to local conditions.

A few assumptions are made here. It is assumed that the most stable arrangements of each defect at static conditions remains the same at high temperatures and that a more stable arrangement does not emerge at high temperature. For the three major H-free species Fe_{Mg}^{X}, V_{Mg}'', and $Fe_{Mg}^{\cdot}$ this assumption was not applied and their energy was calculated in both of their arrangements (on an M1 or M2 site). For each type of defect our model assumes that the relative enthalpy of each defect is equivalent to the relative energy of each defect for the purposes of calculating the configurational entropy of internal arrangements of the defects (with the exception of Fe_{Mg}^{X}, V_{Mg}'', and $Fe_{Mg}^{\cdot}$ where the relative energy is used explicitly). The terms involved here are generally much smaller than the terms of the configurational entropy of the defects spread across the crystal itself (intersite compared to intrasite terms) and thus this assumption is likely valid. We also assume ideality in our reactions and that the concentration of defects is low enough that they are isolated that is, that defect-defect interactions terms are 0 and that the non-configurational energy of each reaction is a linear function of its concentration (first terms in Equation 8). Our model considers olivine in isolation and does not consider its stability against highly oxidized iron phases such as hematite and laihunite which will eventually form as oxidation increases. Critically our model only considers thermodynamic end processes without kinetic effects, as discussed above these could be particularly significant for reactions that must occur at the crystal interface.

2.3. Error Discussion

The largest source of error in our model comes from the fact that it is a completely theoretical model and thus could exclude key mechanisms that occur in real crystals. It also has numerous assumptions and excludes any effect of kinetics. The most accurate way to measure the error is thus by comparison to measurements of real systems. This is very difficult to do however. The relevant defect concentrations are often below 1 ppm and thus are hard to detect directly. Comparisons can be made to measurable properties if these properties can be linked directly to some defect concentration. We have previously done this for an iron-free version of this model and replicated experimental diffusion rates in forsterite (Muir et al., 2021) and hydrogen-bearing (Muir, Zhang, & Walker, 2022) forsterite suggesting our model is accurate at least in iron-free conditions. While there are many measurements of diffusion and conductivity, which are both defect sensitive, in iron-bearing olivine we currently lack an atomistic model to convert our defect concentrations into these properties. Our model does predict, however, that if these properties are sensitive to the concentrations of Mg vacancies, Si vacancies or Ferric iron concentrations then they should exhibit strong non-Arrhenius type behavior with large variations in different P, T, $aSiO_2$ conditions and these variations should be experimentally measurable.

Our calculations also have errors arriving from the use of DFT. This involves a set of systematic errors from using approximations to exchange correlation, not using infinitely large basis sets and k-point grids and in our case from using harmonic expansions. Our model is setup so that we are only concerned with energy differences between different systems and thus most of these systematic errors should cancel out. For example, while the effect of hydrogen can increase anharmonicity in the crystal there is evidence to suggest that this is only in comparison to dry systems and that different H defects have similar anharmonicities (Balan et al., 2017; Yang et al., 2015). Propagating error through our model which contains 44 reactions and is solved numerically rather than analytically is also complicated. We can estimate the error, however, as the oxidation reaction of iron is largely driven by two reactions and the distribution of H is also largely driven by two reactions. All four of these reactions have a strong contribution from configurational entropy which is determined analytically in our model rather than from DFT and so the DFT errors will be of less relevance than normal. To estimate the effect of these errors we applied an estimated "DFT error" of 1.5 meV/atom to these 4 major reactions and propagated this through our model. At sample conditions (1500 K, 5 GPa, -10 fO_2, 0/100 wt. ppm water) a change of $Fe^{3+}/\sum Fe$ of <1.00%/0.39% was seen in dry and wet conditions respectively. This is the error in absolute terms, the relative error (the effect of changing variables) will be less. This means the effect of systematic DFT errors in our system is small and errors in model construction will likely be much more important.
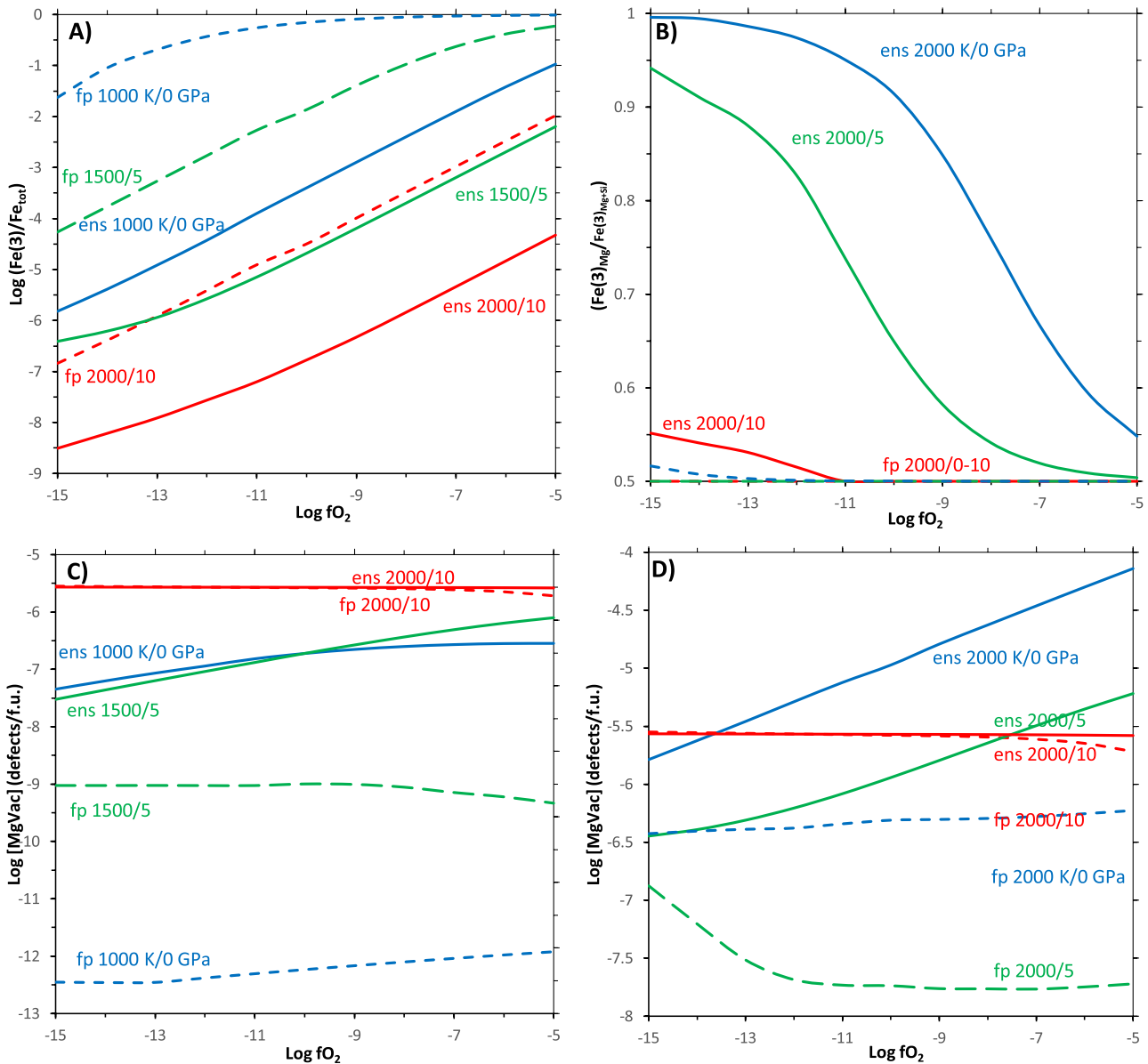
Figure 1. Comparison of (a) $\sum Fe^{3+}/Fe^{tot}$ (b) $\sum Fe^{3+}_{Mg}/Fe^{3+}_{Si+Mg}$ and C-D $\left[V''_{Mg}\right]$ for enstatite buffered (solid line) and fp buffered (dotted line) olivine (Fe# = 0.1) at some selected conditions (temperature K/pressure GPa).

3. Results and Discussion

3.1. Dry Olivine and Comparison to Past Measurements

The two oxidation mechanisms for iron in olivine (Equations 5 and 6) both vary the Mg:Si ratio in olivine and thus have a dependence on αSiO_2. This effect is plotted for some sample conditions in Figure 1 with two different buffers, MgO (fp) and $MgSiO_3$ (ens).

Iron oxidation causes variation in two key factors $\sum Fe^{3+}/Fe^{tot}$ and $\sum Fe^{3+}_{Mg}/Fe^{3+}_{Si+Mg}$. In an MgO buffered regime (low αSiO_2) oxidation is more favored than in an enstatite buffered regime (high αSiO_2) and $\sum Fe^{3+}/Fe^{tot}$ can be over 3 orders of magnitude larger (Figure 1a). In the enstatite buffered system the one site mechanism (Equation 6) (producing Ferric iron on the Mg site) is favored because this mechanism consumes $MgSiO_3$, in the MgO buffered system the two site mechanism (Equation 5) (producing Ferric iron on both the Si and Mg sites) is favored because it consumes MgO. This means that $\sum Fe^{3+}_{Mg}/Fe^{3+}_{Si+Mg}$ is much higher in the enstatite
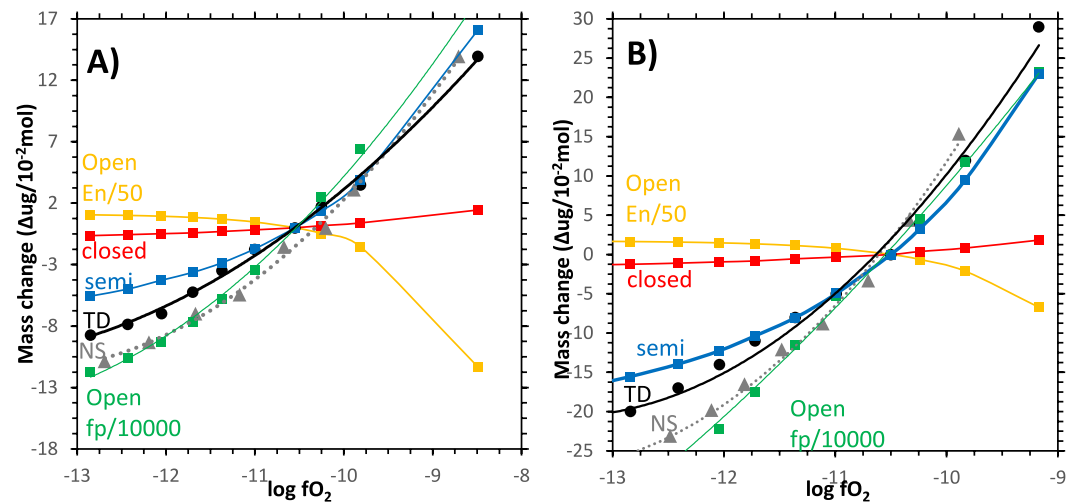
Figure 2. Prediction of how mass in the olivine varies as a function of oxygen fugacity at 1403 K and 0 GPa with (a) Fe# = 0.2 and (b) 0.5. Black and gray lines are experimental measurements of Tsai and Dieckmann (2002) and Nakamura and Schmalzried (1983) respectively while the other lines are our predictions in various systems as explained in the text. The open systems have been divided by 50 (enstatite buffered) and 10,000 (periclase buffered) respectively to fit in the graph.

buffered system (Figure 1b). Thus both the degree and the mechanisms of oxidation of olivine are predicted to be highly sensitive to chemical environment. A similar conclusion was reached in an earlier model by Stocker and Smyth (1978) based around charge neutrality conditions and mass action equations but without considerations of explicit energies. This sensitivity of oxidation will have substantial effects on $\left[V''_{Mg}\right]$ (Figures 1c and 1d) (because the one site mechanism (Equation 6) produces V''_{Mg} while the 2 site mechanism does not) as also predicted by Stocker and Smyth (1978). Contrary to Stocker and Smyth (1978) who predicted a decrease in $\left[V''''_{Si}\right]$ with iron oxidation our model predict increases in $\left[V''''_{Si}\right]$ proportional to the increases in $\left[V''_{Mg}\right]$ though with low overall concentrations (<pptrillion). Such results are important to consider when comparing lab-based with earth-based olivine as the $aSiO_2$ environment in the lab may lead to much higher oxidation than will be seen in the Earth.

The effects of buffers are important when comparing our results to the previous literature. Two previous thermogravimetric studies, Nakamura and Schmalzried (1983) and Tsai and Dieckmann (2002), determined defect concentrations in olivine through mass changes which were then, alongside an array of diffusion measurements, converted into a thermodynamic model of oxidation in Dohmen and Chakraborty (2007). In Figure 2 we compare our predicted mass changes in forsterite with a varying fO_2 to the measured mass changes at the same P, T conditions. Our main model (enstatite buffered) is shown in orange and predicts a change in mass with fO_2 that is both larger (~50 times) and with the opposite sign than the mass change seen in the experimental measurements (black and gray lines). With a MgO buffer (fp-buffered) our model predicts similar trends with fO_2 to the experiment but with mass changes ~1,000 times larger. Our suggested reason for this discrepancy is due to the different αSiO_2 regimes in our model versus the experiments.

In the thermogravimetric studies and in Dohmen and Chakraborty (2007) there was some discussion about the exact thermodynamic conditions of the crystals in question with the actual αSiO_2 conditions of the experiments being unknown. Two possibilities are considered. First is a thermodynamically open system which allows the olivine to act with an external agent (in our case $MgSiO_3$ or MgO) which imposes a fixed αSiO_2 on the crystal and allows variance in the cationic ratio of Mg:Fe:Si. The second case is a thermodynamically closed system where the crystal does not react with any external agents. Strictly some openness is required to allow the introduction of oxygen but we shall define a closed system as one where the cationic ratio is fixed. This is measured through the parameter ξ defined as:

$$\xi = \frac{n_{Si}}{n_{Si} + n_{Fe} + n_{Mg}}$$

where n_{cat} is the number of that cation per formula unit. A perfect olivine has a ξ value of 1/3. In both Nakamura and Schmalzried (1983) and Tsai and Dieckmann (2002) olivine powder was produced from Fe_2O_3, MgO, and SiO_2 and then sintered in the presence of CO/CO_2 gas during which the oxidation occurs. Any leftover starting material at this point could react with the olivine and fix αSiO_2 (and make the system open) but in both cases no other phases could be detected with XRD or SEM making this unlikely. In Nakamura and Schmalzried (1983) the samples were sintered in a Pt capsule. This has no obvious αSiO_2 buffering ability but as pointed out by Tsai and Dieckmann (2002) could introduce Fe dissolved in the Pt into the sample which would complicate the analysis but would not change αSiO_2. In contrast Tsai and Dieckmann (2002) sintered their sample in a quartz capsule which could obviously act as a SiO_2 reagent and make the crystal thermodynamically open. While they could not rule this out they considered a reaction between the quartz capsule and the olivine unlikely due to the small contact area of the quartz and the olivine, no detectable mass change in the quartz and no observed sticking between the olivine and the sample holder after the reaction. Thus they concluded that their reaction was likely thermodynamically closed with a fixed ξ. Our results agree with the conclusion that neither of these systems are open as our model predict much larger mass changes in an open thermodynamic system buffered either by MgO or $MgSiO_3$ than was observed in either of their likely closed systems.

Neither of our two proposed oxidation reactions 5 and 6 can operate in a closed system and thus cannot be operating in a closed experiment. Reaction 24 is one possible closed reaction. This reaction results in a growth of the crystal as seen by the production of a new Mg_2SiO_4 unit which leads to a mass increase but this increase is solely due tp the introduction of oxygen. Such a mechanism doesn't require any external buffer reactions and it keeps the value of ξ fixed so it would fit our definition of a closed cationic system. Reaction 24 is highly unfavored compared to reactions 5 and 6 and thus our model predicts that it will not occur if external αSiO_2 buffers are available to enable these reactions. To test what happens in the absence of these buffers we prevented reactions 5 and 6 from occurring in our model and only allowed oxidation to occur through reaction 24 which produced the red line trace in Figure 2. In this case our model replicates the trends in mass induced by a varying fO_2 that were seen in the experiments but our predicted mass changes are about an order of magnitude smaller. This suggests that either our model lacks some real mass changing process that occurs in the real system (such as a different closed oxidation reaction) or that the αSiO_2 situation in the experiments is more complicated than our "closed" and "open" systems presented here. As an example this could occur if the quartz in the Tsai and Dieckmann (2002) system was reacting with the olivine but very slowly with kinetic limits. This would place the experimental conditions between the thermodynamically open and closed systems proposed here. Regardless our model predicts that the thermodynamically open system has much more favorable reactions with much larger mass changes than the thermodynamically closed system and thus if reactions with an external SiO_2 buffer are available these reactions will dominate the final result and the mechanics of the closed system are irrelevant. In the mantle enstatite is present and thus unless reactions with the enstatite on the grain surface and/or diffusion of the resulting products into the final grain are strongly kinetically limiting, olivine in the mantle should be thermodynamically open and better represented by our enstatite buffered model than the near closed model of Dohmen and Chakraborty (2007). Therefore we shall only present results from an open, enstatite buffered system from now on.

In Figure 3 we examine the predicted values of $\sum Fe^{3+}_{Mg}/Fe^{3+}_{Si+Mg}$, $\left[V''_{Mg}\right]$ and $\sum Fe^{3+}/Fe^{tot}$ against P, T and fO_2. Considering first $\sum Fe^{3+}_{Mg}/Fe^{3+}_{Si+Mg}$ (Figure 3a) which represents the relative dominance of reactions 5 versus 6 our model finds that increasing fO_2 always decreases $\sum Fe^{3+}_{Mg}/Fe^{3+}_{Si+Mg}$ (promotes the two site mechanism (Equation 5)). Increasing the pressure initially decreases $\sum Fe^{3+}_{Mg}/Fe^{3+}_{Si+Mg}$ (promoting the one site mechanism (Equation 6)) and then increases it. Increasing the temperature is predicted to both increase $\sum Fe^{3+}_{Mg}/Fe^{3+}_{Si+Mg}$ (low pressure) and decrease it (high pressure). Similar trends can be seen in $\left[V''_{Mg}\right]$ (Figure 3b) and the related $[V''''_{Si}]$ with mechanisms that promote the one site mechanism (reaction 6) also increasing $\left[V''_{Mg}\right]$ but in this case the dominant variable is pressure as the formation of a large V''_{Mg} defect becomes increasingly disfavored by pressure.

Our predicted values of $\sum Fe^{3+}/Fe^{tot}$ are shown in Figure 3c. The value of $\sum Fe^{3+}/Fe^{tot}$ varies by over 10 orders of magnitude across the calculated pressure, temperature and fO_2 ranges. Unsurprisingly the largest control on $\sum Fe^{3+}/Fe^{tot}$ is oxygen fugacity. Increasing fO_2 from log -15 to -5 can lead to $\sum Fe^{3+}/Fe^{tot}$ increases of over 4 orders of magnitude. Increasing the pressure generally decreases $\sum Fe^{3+}/Fe^{tot}$ while increasing the temperature raises $\sum Fe^{3+}/Fe^{tot}$.
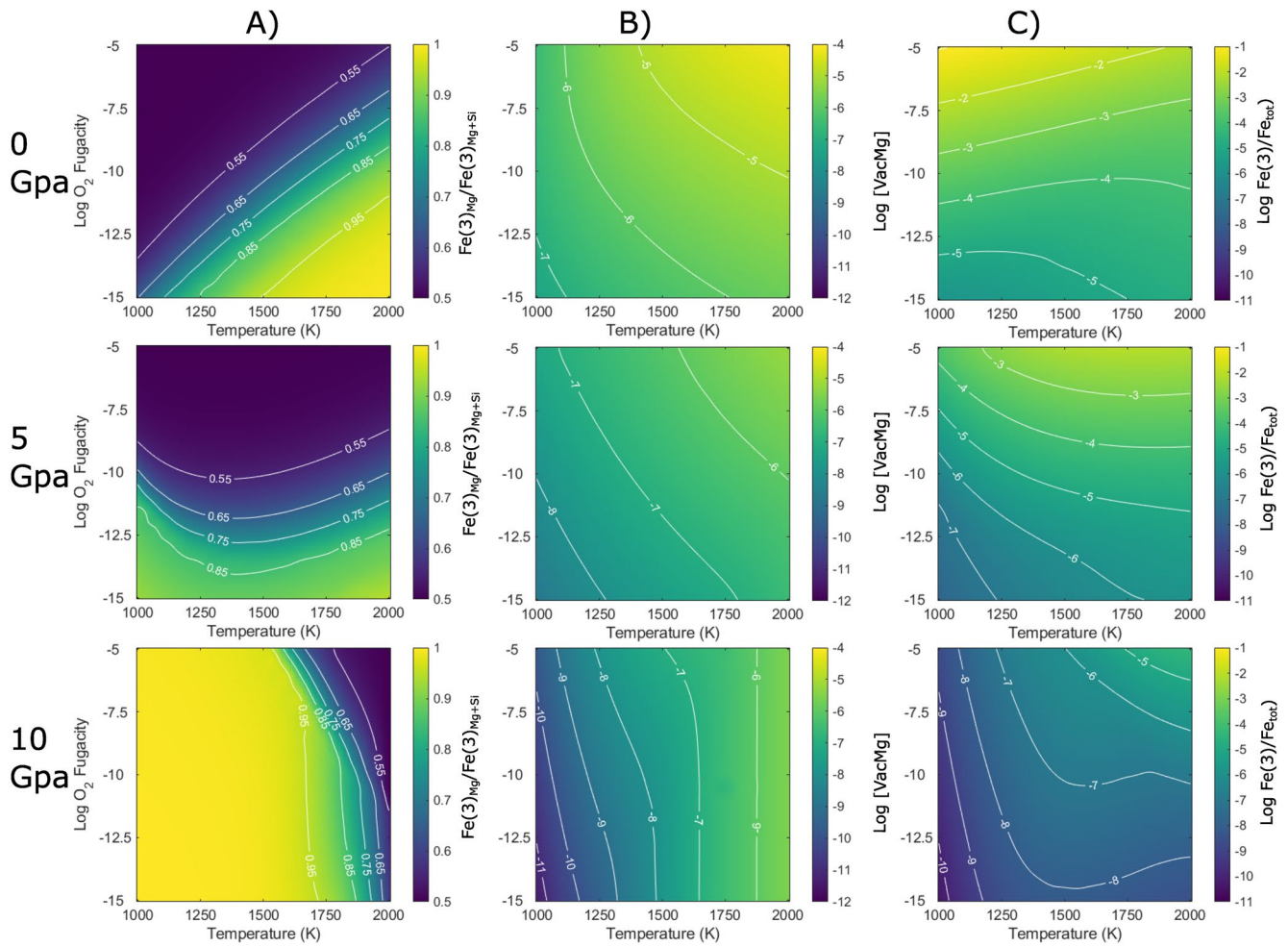
Figure 3. Plot of varying (a) $\sum Fe^{3+}_{Mg}/Fe^{3+}_{Si+Mg}$ (b) $Log\left[V''_{Mg}\right]$ and (c) $Log \sum Fe^{3+}/Fe^{tot}$ in pure olivine with Fe# = 0.1 as a function of log fO_2 and temperature at three different pressures. Points were calculated every 50 K and 0.5 log fugacity and then interpolated using spline inter2p in MATLAB, individual points for this can be found in the supplementary spreadsheet.
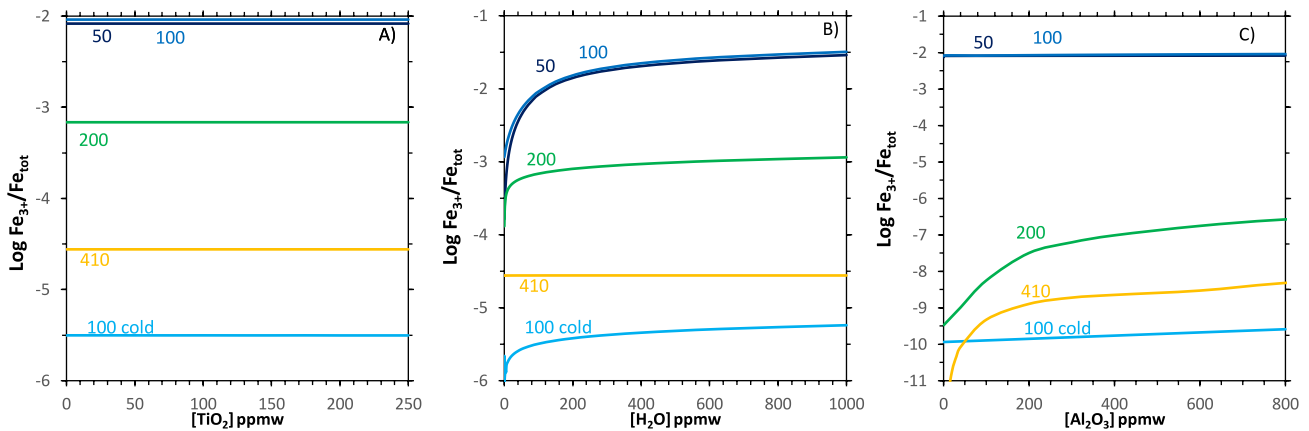

Figure 4. Variation in oxidation ($\sum Fe^{3+}_{Mg}/Fe^{3+}_{Si+Mg}$) at selected depths in the mantle (50, 100, 200 and 410 km with temperatures and fO_2 fit to an oceanic geotherm or a continental geotherm for 100 cold see Table S1) as a function of $[TiO_2]$, $[H_2O]$ or $[Al_2O_3]$. In each figure one of these concentrations is varied and the other two were set to 165/100/800 ppmw respectively to demonstrate the effect of these species even when other interacting species are highly concentrated. Fe# was 0.1.

Thus our model finds that both the amount of oxidation ($\sum Fe^{3+}/Fe^{tot}$) and the products relating to the specific mechanism of that oxidation ($\sum Fe_{Mg}^{3+}/Fe_{Si+Mg}^{3+}$ and $\left[V''_{Mg} \right]$) have a complex dependence on P, T, and fO_2. This means that great care needs to be taken when extrapolating measurements of olivine oxidation or properties dependent upon olivine oxidation products, such as diffusion, to ranges beyond where they are measured. Point defect models such as those of Dohmen and Chakraborty ([2007]) can therefore only provide information upon the temperatures (1273–1553 K), fO_2 (−13 to −9, pressures (0 GPa) and αSiO_2 where they are measured and cannot reliably be used in other conditions of the mantle.

Some other iron products are possible in our model such as $\left\{ Fe_{Mg}^{\cdot}Fe_{Mg}^{\cdot}V''_{Mg} \right\}^{\times}$ which can be produced by reaction 12, $Fe_I^{\cdot\cdot}$ by reaction 10 and $Fe_I^{\cdot\cdot\cdot}$ by reaction 11. Our model does not predict large concentrations of any of these products with the maximum concentrations produced across the conditions in Figure 3 being 9.2×10^{-8}, 2.4×10^{-6}, and 4.7×10^{-14} defects/f. u. respectively. Thus we shall ignore these products from now on.

3.2. The Effect of Other Elements

If considered as a deviation from forsterite, iron is by far the most common defect element in olivine (De Hoog et al., [2010]) but it is possible that other defective elements present in smaller concentrations may change the oxidation reactions of iron. We shall consider three defects that are present in reasonable concentrations in olivine, Ti, Al and water (as H-bearing defects). Figure 4 shows how varying the concentration of these elements varies the oxidation of iron and its products at different mantle depths.

Considering first Ti (Figure 4a) our model finds no relationship between [Ti] and iron oxidation at any depth conditions in the mantle. This is perhaps unsurprising as our model has no direct Ti-Fe relationship and it is unclear what such a relationship would entail. Ti does change the configurational entropy and interacts with H (which can also affect Fe oxidation Figure 4b) but these effects are not significant as the concentration of Fe is much greater than the concentration of Ti. This lack of effect of Ti on iron oxidation is expected to hold for all defective elements which have a much lower concentration than Fe and which do not interact directly with it.

The presence of H allows the formation of $\left\{ Fe_{Mg}^{\cdot}H'_{Mg} \right\}^{\times}$ pairs which increases the amount of Ferric iron that is present. This increase is initially sharp with small amounts of water leading to large increases in Ferric iron before this trend levels off (but still increases) as $[H_2O]_{bulk}$ increases. This effect is strongest at the lowest pressures and is eliminated once the bottom of the upper mantle (410 km) is reached. In iron-free systems increasing the pressure increases the favourability of $(4H)_{Si}^{\times}$ (Muir, Jollands, et al., [2022]) and our model finds that this relationship also holds against $\left\{ Fe_{Mg}^{\cdot}H'_{Mg} \right\}^{\times}$. At 410 km depth our model predicts that less than 0.01% of the water is not in $(4H)_{Si}^{\times}$ and thus $\left\{ Fe_{Mg}^{\cdot}H'_{Mg} \right\}^{\times}$ does not form to any significant degree at the base of the upper mantle. Our model thus predicts that wet olivine should have significantly more (up to 2 orders of magnitude) Ferric iron than dry olivine at shallow regions but in deeper regions this effect should be less important and should be non-existent at the base of the upper mantle.

FTIR studies have shown a strong band at 3,350 cm^{-1} in hydrated Fe-containing olivine which has been attributed to an $\left\{ Fe_{Mg}^{\cdot}H'_{Mg} \right\}^{\times}$ defect Berry et al. ([2007]). Our model agrees with this assessment as it predicts that over 99.999% of the water in olivine adopts this structure in the conditions of the experiment (1673 K, 1.5 GPa, 1 wt% $Fe2O3$, 42 wt ppm H2O, NNO+9, enstatite buffered). Our model predicts that these measurements will not hold throughout the mantle, however, and that increasing pressure for example, from 1.5 to 11.5 GPa drops the favourability of $\left\{ Fe_{Mg}^{\cdot}H'_{Mg} \right\}^{\times}$ such that it takes <0.00001% of the water. In Berry et al. ([2007]) this Fe-H structure was suggested to be an associated pair. We calculated the dissociation reaction 17 and found it be highly unfavorable. Agreeing with the experimental interpretation our calculations predict that essentially all $\left\{ Fe_{Mg}^{\cdot}H'_{Mg} \right\}^{\times}$ occurs as associated pairs. This should have strong effects on the diffusion rate of H if significant amounts of $\left\{ Fe_{Mg}^{\cdot}H'_{Mg} \right\}^{\times}$ are formed as hydrogen in this Fe-H structure should be slower to diffuse than hydrogen in other defects.

In Figure 4c our model considers the effect of Al which allows for the formation of $\left\{ Fe_{Mg}^{\cdot}Al'_{Si} \right\}^{\times}$ pairs. Al has similar behavior to H with Al increasing Fe oxidation (at first rapidly and then slowly) but with an opposite pressure derivative as the Al effect only occurs with increasing depth and is only significant at large depths. The formation reaction of $\left\{ Fe_{Mg}^{\cdot}Al'_{Si} \right\}^{\times}$ is favored by increasing pressure and temperature (Table 1) which both
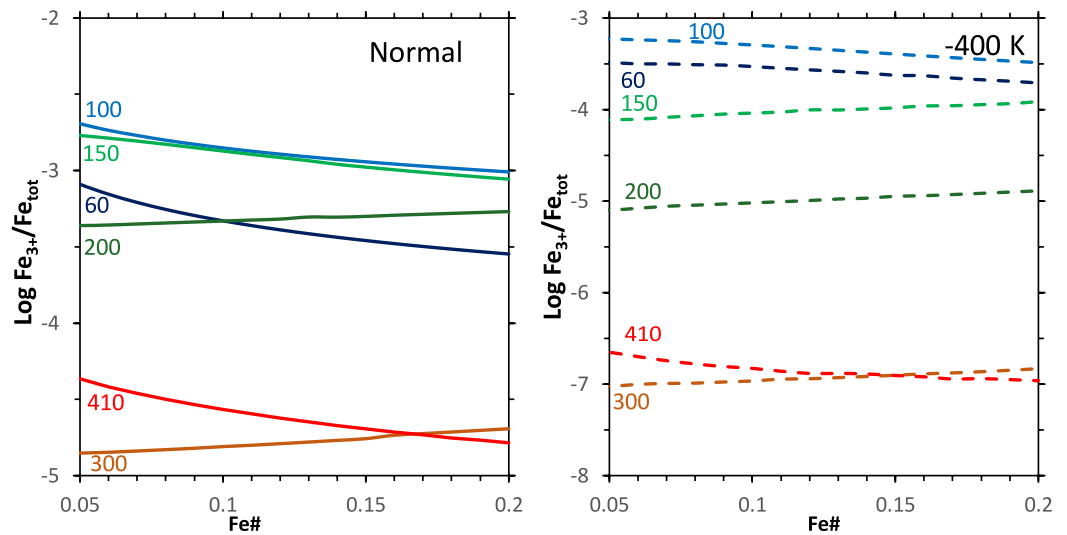
Figure 5. Variation in $\sum Fe^{3+}_{Mg}/Fe^{3+}_{Si+Mg}$ as a function of Fe# at specific depths in the mantle. In each case we use the temperature, $[Al_2O_3]$, $[TiO_2]$ and $[H_2O]_{bulk}$ contents projected along an oceanic geotherm found in Table S1 (left) or -400 K (right) with concentrations adjusted appropriately.

increase with depth though pressure is the largest control. This is again a large effect which can increase iron oxidation by over 2 orders of magnitude.

Our model also demonstrates the effect of temperature in Figure 5b by considering a colder region of the mantle. This cold region has similar trends to the hotter normal mantle but with lower total iron oxidation. A decrease of 400 K leads to a decrease in $\sum Fe^{3+}/Fe^{tot}$ of roughly 2 log units.

Finally our model consider the effect of varying Fe# as olivine can have varying amounts of base iron. This is plotted in Figure 5a. Our model finds that, regardless of depth, variations in Fe# lead to only small changes in iron oxidation. Slight increases in oxidation are seen at mid depths ($\sim$200–300 km) and slight decreases at shallow ($<$200 km) or deep ($>$300 km) depths but never by more than 0.5 of a log unit. This effect is small compared to other possible effects on iron oxidation such as water or Al or temperature.
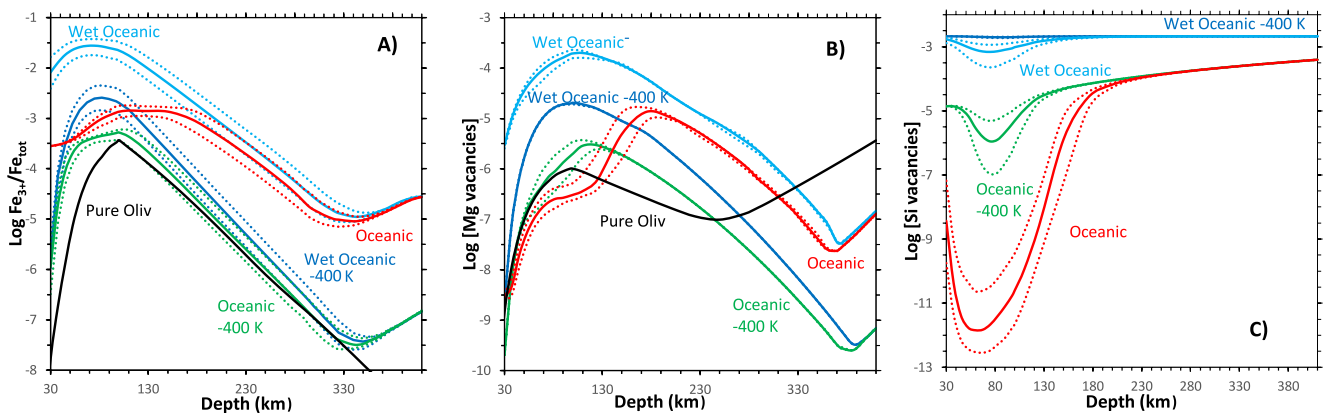

Figure 6. Predicted (a) $\sum Fe^{3+}_{Mg}/Fe^{3+}_{Si+Mg}$ (b) Concentration of Mg vacancies ($(2H)^{\times}_{Mg} + H'_{Mg} + V''_{Mg}$ excluding $\left\{ Fe^{\cdot}_{Mg}H'_{Mg} \right\}^{\times}$) and (c) Si vacancies ($(4H)^{\times}_{Si} + V''''_{Si} + (3H)'_{Si}$) as a function of depth for various systems. In each case there is an oceanic geotherm or the geotherm minus -400 K with $[TiO_2]$ and $[Al_2O_3]$ values taken from our derivations in Table S1 and adjusted for temperature in the cold system. An exception is the black line which is pure olivine (no Ti, Al or water) along an oceanic geotherm, in graph C this line is below -14.8 for all conditions. Fe# = 0.1 for all systems. Water is either taken using the values in Table S1 or in the "wet" system is fixed to 500 ppmw. The dotted lines represent an increase or decrease in log fO_2 by 1 unit from the value in Table S4.

4. Geophysical Implications

In Figure 6a we plot the predicted oxidation of iron along upper mantle geotherms with realistic Ti and Al concentration depth profiles (Table S1 in Supporting Information S1). For water we show both a "standard" olivine whereby the water concentration increases with depth and is based upon geophysical observations (Demouchy and Bolfan-Casanova, 2016) and then a second "wet" olivine whereby the water is always set to 500 ppmw and represents an olivine that has been locally enriched with a lot of water. Two key predictions arise from this model.

The first key prediction is that depth is a strong control on iron oxidation but it is extremely nonmonotonic. With increasing depth oxidation at first increases sharply reaching a maximum at ~100 km then it begins to decrease and then it increases sharply again. This behavior occurs in "normal" olivine, in wet olivine and even in pure forsterite ($[Ti],[Al],[H_2O]_{bulk} = 0$) and is due to the interplay of varying P, T, and fO_2 rather than any extrinsic defect interactions. Over the depth of the upper mantle iron oxidation can vary by 2 orders of magnitude in normal olivine and by over 3 orders in wet olivine which affirms that there is no standard iron oxidation state of olivine in the mantle. Wet olivine behaves similarly to "normal" olivine but has a larger and earlier peak in Ferric iron concentration before becoming increasingly similar with depth as $(4H)^\times_{Si}$ (which does not interfere with iron oxidation) becomes the dominant water product.

As iron oxidation effect is strongly dependent upon fO_2 and fO_2 is poorly constrained in the mantle our model show bounds to indicate the effects of changing fO_2 by ± 1 log bar unit. Generally our model finds this to be a minor effect and with the absence of large local variations in fugacity/large differences between our modeled fO_2 and real mantle fO_2, the temperature or the water content of olivine will have much larger effects on iron oxidation in olivine than fO_2. The shape of our iron oxidation versus depth chart is robust to even quite large changes to fO_2 as our model predicts iron oxidation is strongly driven by pressure.

In Figure 6 our model also shows the effect of temperature. Our standard fitting is to an oceanic geotherm but parts of the mantle may be cooler than this and we demonstrate the effects of this by arbitrarily removing 400 K from our standard geotherm. Rather than representing any one specific mantle structure this is to show that temperature has a very large effect which cannot be extrapolated through Arrhenius type equations and that every specific temperature context needs to be considered on its own. In a colder region of the mantle less oxidation is seen with oxidation decreasing by over an order of magnitude when the temperature drops by 400 K. In such colder regions the shape of the depth versus oxidation curve is very similar to that seen at normal mantle temperatures but the effect of depth is more pronounced with the total amount of iron oxidation now varying by up to 5 orders of magnitude over mantle depths.

The nonmonotonic behavior of oxidation makes fitting iron oxidation as a function of depth very difficult. Standard formulations like Arrhenius fitting simply will not suffice and due to the effect of multiple variables operating upon multiple equations a fitting that is both thermodynamically rigorous and simple may be impossible. The oxidation state of iron against depth can be approximated by fitting a fourth-order polynomial but this is provided simply as an empirical means to replicate our results and is not a rigorous thermodynamic fitting. Our model predictions were thus fit to the following equation:

$$\log var = xd^4 + yd^3 + zd^2 + ad + b \tag{24}$$

where d is depth in km and var is the variable of interest either $\sum Fe^{3+}_{Mg}/Fe^{3+}_{Si+Mg}$ or [Mg vacancies] or [Si vacancies]. The results are shown in Table 2.

The second key finding is that iron oxidation is generally small. In "normal" olivine $\sum Fe^{3+}_{Mg}/Fe^{3+}_{Si+Mg}$ never exceeds 0.003 while even in our wet olivine this does not exceed 0.03. This matches with observations in recovered rocks where Ferric iron was found to be near or below the limit (~0.01) of Mossbauer spectroscopy (Banfield et al., 1990; Canil et al., 1994; Ejima et al., 2012, 2013, 2018; McCammon et al., 2004; McGuire et al., 1991). It should be noted that due to the strong depth dependence of oxidation uplifted rocks could lose considerable amounts of Ferric iron from their peak oxidation state at ~100 km if they have time to reequilibrate during uplift and thus such rocks may only sample the shallowest conditions of the mantle.

Despite iron oxidation being objectively small our model predicts that it can have large effects on the defect structure of olivine and thus on properties that depend on those defects. This is shown in Figures 6b and 6c where we plot the varying concentration of Mg and Si vacancies predicted by our model. In each case our we consider only defects that are relatively mobile to consider properties that rely upon diffusion of these defects.

Table 2
Fitting to Equation 3 for the Depth Profiles in Figure 6

		Oceanic	Oceanic −400 K	Wet oceanic	Wet oceanic −400 K
$\text{Log}\left[\sum \text{Fe}^{3+}_{\text{Mg}}/\text{Fe}^{3+}_{\text{Si+Mg}}\right]$	x	6.17×10^{-10}	-1.46×10^{-9}	-1.88×10^{-10}	-1.95×10^{-9}
	y	-2.11×10^{-7}	1.86×10^{-6}	4.77×10^{-7}	2.32×10^{-6}
	z	-7.39×10^{-5}	-7.66×10^{-4}	-2.49×10^{-4}	-9.13×10^{-4}
	a	2.31×10^{-2}	1.04×10^{-1}	3.06×10^{-2}	1.21×10^{-1}
	b	-4.32	-7.69	-2.69	-7.63
Log [Mg vacancies]	x	1.89×10^{-9}	-1.37×10^{-9}	-2.12×10^{-10}	-2.09×10^{-9}
	y	-1.36×10^{-6}	1.71×10^{-6}	4.89×10^{-7}	2.31×10^{-6}
	z	2.10×10^{-4}	-7.51×10^{-4}	-2.98×10^{-4}	-9.16×10^{-4}
	a	1.60×10^{-2}	1.21×10^{-1}	5.28×10^{-2}	1.34×10^{-1}
	b	-8.83	-11.78	-6.53	-10.91
Log [Si vacancies]	x	7.94×10^{-9}	1.93×10^{-9}	6.30×10^{-10}	4.67×10^{-11}
	y	-7.32×10^{-6}	-1.81×10^{-6}	-5.88×10^{-7}	-4.46×10^{-8}
	z	2.17×10^{-3}	5.58×10^{-4}	1.80×10^{-4}	1.43×10^{-5}
	a	-1.98×10^{-1}	-5.67×10^{-2}	-1.90×10^{-2}	-1.65×10^{-3}
	b	-5.75	-3.65	-2.42	-2.63

In the Mg case we have included $(2H)^{\times}_{\text{Mg}}$ H'_{Mg} and V''_{Mg} which are expected to be relatively mobile (Muir et al., 2021; Muir, Zhang, & Walker, 2022) but have excluded $\left\{\text{Fe}^{\cdot}_{\text{Mg}}H'_{\text{Mg}}\right\}^{\times}$ as this is expected to be less mobile. In the Si case we consider $(4H)^{\times}_{\text{Si}}$, $(3H)'_{\text{Si}}$ and V''''_{Si}.

For Mg vacancies (Figure 6b) our model predicts a steady increase in concentration as depth increases up to around 100 km before a sharp decrease and then a small increase at the very bottom of the upper mantle. This behavior is largely controlled by water rather than iron oxidation and is similar to the traces found in iron-free wet forsterite (Muir, Jollands, et al., 2022). In a water-free system (black line in Figure 5b) the vacancy concentration is controlled entirely by iron oxidation and a peak is still seen around 100 km but this is followed by a shallow decrease and then a further increase with depth to a new peak at 410 km. Our predicted "wet" behavior occurs even in samples with "natural" water concentrations between 3 and 93 ppmw which shows that only small amounts of water are required to control this system. Increasing the water concentration or the temperature increases the total Mg vacancy concentration at any depth with both of these effects leading to potentially an increase of over 1 log unit. As Mg diffusion can control conductivity and possibly crystal faceting our model predicts that these properties can vary heavily with depth in the upper mantle due to the related changes in iron oxidation.

For Si vacancies (Figure 6c) our model predicts extremely low concentrations in the absence of water. V''''_{Si} in the dry system are produced largely through the conversion of Mg vacancies created mostly from iron oxidation (with a small contribution for the Mg Frenkel reaction) but this is not particularly favorable according to our model. In the wet system, however, large amounts of $(4H)^{\times}_{\text{Si}}$ are produced. Similar to Mg vacancies the total amount of $(4H)^{\times}_{\text{Si}}$ produced is largely controlled by the water concentration with iron oxidation having a strong effect on the shape of the depth versus concentration trace. $[(4H)^{\times}_{\text{Si}}]$ is predicted to gradually increase with depth due to pressure favoring this defect but with potentially a large decrease in concentration centered around a depth of 60–70 km. This decrease is related to the production of $\left\{\text{Fe}^{\cdot}_{\text{Mg}}H'_{\text{Mg}}\right\}^{\times}$ (and some $(2H)^{\times}_{\text{Mg}}$ though this is more favored at 100 km see Figure 4b) which is favored at the lower pressures and the moderate temperatures that exist around 70 km depth. As water concentration increases $(4H)^{\times}_{\text{Si}}$ is favored relatively (Muir, Jollands, et al., 2022) which decreases the magnitude of the dip at 70 km. Decreasing the overall temperature also increase the favorability and the concentration of $(4H)^{\times}_{\text{Si}}$

$[(4H)^{\times}_{\text{Si}}]$ likely controls Si diffusion which likely controls the strength of olivine though there is still some debate about the possible role of O diffusion on the strength of oli $(4H)^{\times}_{\text{Si}}$.vine (Costa & Chakraborty, 2008). Assuming this relationship is true our model predicts wildly different potential olivine strengths in the upper mantle with

$[(4H)^\times_{Si}]$ and thus Si diffusion varying by potentially 10 orders of magnitude in different plausible conditions. We predict that very wet and very cold olivine will have consistent $[(4H)^\times_{Si}]$ and thus Si diffusion and strength throughout the depth range of the mantle. We predict, however, that olivines with "normal" concentrations of water will have a sharply varying strength in the mantle with a strong weakening around 70 km depth followed by a strengthening as depth increases. Such strength changes will undoubtedly have an effect on mantle rheology. The exact relationship between $[(4H)^\times_{Si}]$ and Si diffusion rates and between Si diffusion rates and olive strength needs to be clarified before the actual strength of olivine in the mantle can be calculated but it is highly unlikely to be static with depth.

5. Conclusion

All of the thermodynamically favored oxidation reactions rely upon reactions with external products (such as MgO, SiO_2, $MgSiO_3$, and O_2). These reactions can only occur at crystal surfaces and thus require heavy diffusion into and out of the bulk to operate which puts kinetic limits on their operation. In our model we have assumed thermodynamic equilibrium and that the timeframe of mantle processes is long enough that the kinetics of these reactions are unnecessary. This may not always be the case and if mantle rocks have kinetic limits to their oxidation, then the situation will be even more complicated than is sketched here. Uplifted rocks could plausibly maintain deep mantle oxidation if the kinetics are slow enough and the uplift is fast enough. It is difficult to fully speculate as we do not know the diffusivity of all the involved species here to sufficient accuracy but this would be a promising line of future work. Our model predicts large differences between oxidation of shallow and deep rocks and/or rocks processed at low and high pressures and/or low and high SiO_2 in the lab and so comparisons between our calculated data and measured data of rocks at different conditions should be a good guide as to whether kinetics is a large control on these systems and to the accuracy of our models.

Data Availability Statement

Data produced to make Figure 3 as well as supplementary information on methods and energies generated to use in our model can be found at https://osf.io/xjc95/. All DFT results were generated by CASTEP, a commercial program available under academic license that can be found at http://www.castep.org/.

References

Babushkina, M. S., Nikitina, L. P., Goncharov, A. G., & Ponomareva, N. I. (2009). Water in the structure of minerals from mantle peridotites as controlled by thermal and redox conditions in the upper mantle. *Geology of Ore Deposits*, *51*(8), 712–722. https://doi.org/10.1134/s1075701509080042

Balan, E., Blanchard, M., Lazzeri, M., & Ingrin, J. (2017). Theoretical Raman spectrum and anharmonicity of tetrahedral OH defects in hydrous forsterite. *European Journal of Mineralogy*, *29*(2), 201–212. https://doi.org/10.1127/ejm/2017/0029-2599

Banfield, J. F., Veblen, D. R., & Jones, B. F. (1990). Transmission electron-microscopy of subsolidus oxidation and weathering of olivine. *Contributions to Mineralogy and Petrology*, *106*(1), 110–123. https://doi.org/10.1007/bf00306412

Berry, A. J., O'Neill, H. S. C., Hermann, J., & Scott, D. R. (2007). The infrared signature of water associated with trivalent cations in olivine. *Earth and Planetary Science Letters*, *261*(1–2), 134–142. https://doi.org/10.1016/j.epsl.2007.06.021

Blundy, J., Melekhova, E., Ziberna, L., Humphreys, M. C. S., Cerantola, V., Brooker, R. A., et al. (2020). Effect of redox on Fe-Mg-Mn exchange between olivine and melt and an oxybarometer for basalts. *Contributions to Mineralogy and Petrology*, *175*(11), 103. https://doi.org/10.1007/s00410-020-01736-7

Campbell, A. J., Danielson, L., Righter, K., Seagle, C. T., Wang, Y. B., & Prakapenka, V. B. (2009). High pressure effects on the iron-iron oxide and nickel-nickel oxide oxygen fugacity buffers. *Earth and Planetary Science Letters*, *286*(3–4), 556–564. https://doi.org/10.1016/j.epsl.2009.07.022

Canil, D., Oneill, H. S., Pearson, D. G., Rudnick, R. L., Mcdonough, W. F., & Carswell, D. A. (1994). Ferric iron in peridotites and mantle oxidation-states. *Earth and Planetary Science Letters*, *123*(1–3), 205–220. https://doi.org/10.1016/0012-821x(94)90268-2

Clark, S. J., Segall, M. D., Pickard, C. J., Hasnip, P. J., Probert, M. J., Refson, K., & Payne, M. C. (2005). First principles methods using CASTEP [Software]. Zeitschrift fuer Kristallographie, *220*(5–6), 567–570. https://doi.org/10.1524/zkri.220.5.567.65075

Cline, C. J., Faul, U. H., David, E. C., Berry, A. J., & Jackson, I. (2018). Redox-influenced seismic properties of uppermantle olivine. *Nature*, *555*(7696), 355–+. https://doi.org/10.1038/nature25764

Costa, F., & Chakraborty, S. (2008). The effect of water on Si and O diffusion rates in olivine and implications for transport properties and processes in the upper mantle. *Physics of the Earth and Planetary Interiors*, *166*(1–2), 11–29. https://doi.org/10.1016/j.pepi.2007.10.006

Dai, L., & Karato, S.-I. (2020). Electrical conductivity of Ti-bearing hydrous olivine aggregates at high temperature and high pressure. *Journal of Geophysical Research: Solid Earth*, *125*(10). https://doi.org/10.1029/2020jb020309

Davis, F. A., & Cottrell, E. (2021). Partitioning of Fe_2O_3 in peridotite partial melting experiments over a range of oxygen fugacities elucidates ferric iron systematics in mid-ocean ridge basalts and ferric iron content of the upper mantle. *Contributions to Mineralogy and Petrology*, 176.

De Hoog, J. C. M., Gall, L., & Cornell, D. H. (2010). Trace-element geochemistry of mantle olivine and application to mantle petrogenesis and geothermobarometry. *Chemical Geology*, *270*(1–4), 196–215. https://doi.org/10.1016/j.chemgeo.2009.11.017

Demouchy, S., & Bolfan-Casanova, N. (2016). Distribution and transport of hydrogen in the lithospheric mantle: A review. *Lithos*, *240*, 402–425. https://doi.org/10.1016/j.lithos.2015.11.012

Dohmen, R., & Chakraborty, S. (2007). Fe-Mg diffusion in olivine II: Point defect chemistry, change of diffusion mechanisms and a model for calculation of diffusion coefficients in natural olivine. *Physics and Chemistry of Minerals*, *34*(8), 409–430. https://doi.org/10.1007/s00269-007-0185-3

Ejima, T., Akasaka, M., Nagao, T., & Ohfuji, H. (2012). Oxidation state of Fe in olivine in andesitic scoria from Kasayama volcano, Hagi, Yamaguchi Prefecture, Japan. *Journal of Mineralogical and Petrological Sciences*, *107*(6), 215–225. https://doi.org/10.2465/jmps.120605

Ejima, T., Akasaka, M., Nagao, T., & Ohfuji, H. (2013). Oxidation states of Fe and precipitates within olivine from orthopyroxene-olivine-clinopyroxene andesite lava from Kasayama volcano, Hagi, Yamaguchi, Japan. *Journal of Mineralogical and Petrological Sciences*, *108*(1), 25–36. https://doi.org/10.2465/jmps.120621a

Ejima, T., Osanai, Y., Akasaka, M., Adachi, T., Nakano, N., Kon, Y., et al. (2018). Oxidation states of Fe in constituent minerals of a spinel lherzolite xenolith from the Tariat depression, Mongolia: The significance of Fe^{3+} in olivine. *Minerals*, *8*(5), 204. https://doi.org/10.3390/min8050204

Frost, D. J., & Mccammon, C. A. (2008). The redox state of Earth's mantle. *Annual Review of Earth and Planetary Sciences*, *36*(1), 389–420. https://doi.org/10.1146/annurev.earth.36.031207.124322

Holland, T. J. B., & Powell, R. (2011). An improved and extended internally consistent thermodynamic dataset for phases of petrological interest, involving a new equation of state for solids. *Journal of Metamorphic Geology*, *29*(3), 333–383. https://doi.org/10.1111/j.1525-1314.2010.00923.x

Knafelc, J., Filiberto, J., Ferre, E. C., Conder, J. A., Costello, L., Crandall, J. R., et al. (2019). The effect of oxidation on the mineralogy and magnetic properties of olivine. *American Mineralogist*, *104*(5), 694–702. https://doi.org/10.2138/am-2019-6829

Kroger, F. A., & Vink, H. J. (1956). Relations between the concentrations of imperfections in crystalline solids. *Solid State Physics*, *3*, 307–435.

Lide, D. E. (2010). *CRC handbook of chemistry and physics* (90th ed.). CRC Press/Taylor and Francis.

Mackwell, S. (2008). Rheological consequences of redox state. In G. J. MACPHERSON, D. W. MITTLEFEHLDT, J. H. JONES, & S. B. SIMON (Eds.), *Oxygen in the solar system*.

Mccammon, C. A., Stachel, T., & Harris, J. W. (2004). Iron oxidation state in lower mantle mineral assemblages - II. Inclusions in diamonds from Kankan, Guinea. *Earth and Planetary Science Letters*, *222*(2), 423–434. https://doi.org/10.1016/j.epsl.2004.03.019

Mcguire, A. V., Dyar, M. D., & Nielson, J. E. (1991). Metasomatic oxidation of upper mantle peridotite. *Contributions to Mineralogy and Petrology*, *109*(2), 252–264. https://doi.org/10.1007/bf00306483

Muir, J. M. R., Chen, Y., Liu, X., & Zhang, F. (2022). Extremely stable, highly conductive boron-hydrogen complexes in forsterite and olivine. *Journal of Geophysical Research: Solid Earth*, *127*(6), e2022JB024299. https://doi.org/10.1029/2022jb024299

Muir, J. M. R., Zhang, F., & Walker, A. M. (2022). Fast anisotropic Mg and H diffusion in wet forsterite. *Physics and Chemistry of Minerals*, *49*(8), 31. https://doi.org/10.1007/s00269-022-01204-7

Muir, J. M. R., Jollands, M., Zhang, F., & Walker, A. M. (2022). Controls on the distribution of hydrous defects in forsterite from a thermodynamic model. *Physics and Chemistry of Minerals*, *49*(4), 7. https://doi.org/10.1007/s00269-022-01182-w

Muir, J., Zhang, F., & Walker, A. M. (2021). The mechanism of Mg diffusion in forsterite and the controls on its anisotropy. *Physics of the Earth and Planetary Interiors*, *321*, 106805. https://doi.org/10.1016/j.pepi.2021.106805

Nakamura, A., & Schmalzried, H. (1983). On the nonstoichiometry and point-defects of olivine. *Physics and Chemistry of Minerals*, *10*(1), 27–37. https://doi.org/10.1007/bf01204323

O'Neill, H. S. (1987). Quartz-fayalite-iron and quartz-fayalite-magnetite equilibria and the free-energy of formation of fayalite (Fe_2SiO_4) and magnetite (Fe_3O_4). *American Mineralogist*, *72*, 67–75.

Stocker, R. L., & Smyth, D. M. (1978). Effect of enstatite activity and oxygen partial-pressure on point-defect chemistry of olivine. *Physics of the Earth and Planetary Interiors*, *16*(2), 145–156. https://doi.org/10.1016/0031-9201(78)90085-7

Tsai, T. L., & Dieckmann, R. (2002). Variation of the oxygen content and point defects in olivines, $(Fe_xMg_{1-x})_2SiO_4$, $0.2 <= x <= 1.0$. *Physics and Chemistry of Minerals*, *29*, 680–694. https://doi.org/10.1007/s00269-002-0283-1

Yang, Y., Wang, Z., Smyth, J. R., Liu, J., & Xia, Q. (2015). Water effects on the anharmonic properties of forsterite. *American Mineralogist*, *100*(10), 2185–2190. https://doi.org/10.2138/am-2015-5241

References From the Supporting Information

Creighton, S., Stachel, T., Eichenberg, D., & Luth, R. W. (2010). Oxidation state of the lithospheric mantle beneath Diavik diamond mine, central Slave craton, NWT, Canada. *Contributions to Mineralogy and Petrology*, *159*, 645–657.

Green, D. H., & Ringwood, A. E. (1970). Mineralogy of peridotitic compositions under upper mantle conditions. *Physics of the Earth and Planetary Interiors*, *3*, 359–371.

Mccammon, C., & Kopylova, M. G. (2004). A redox profile of the Slave mantle and oxygen fugacity control in the cratonic mantle. *Contributions to Mineralogy and Petrology*, *148*, 55–68.

Mccammon, C. A., Griffin, W. L., Shee, S. R., & O'Neill, H. S. C. (2001). Oxidation during metasomatism in ultramafic xenoliths from the Wesselton kimberlite, South Africa: Implications for the survival of diamond. *Contributions to Mineralogy and Petrology*, *141*, 287–296.

Monkhorst, H. J., & Pack, J. D. (1976). Special points for Brillouin-zone integrations. *Physical Review B*, *13*, 5188–5192.

Perdew, J. P., Burke, K., & Ernzerhof, M. (1996). Generalized gradient approximation made simple. *Physical Review Letters*, *77*, 3865–3868.

Woodland, A. B., & Koch, M. (2003). Variation in oxygen fugacity with depth in the upper mantle beneath the Kaapvaal craton, Southern Africa. *Earth and Planetary Science Letters*, *214*, 295–310.